OPTICS CONTINUUM

Optical system characterization in Fourier ptychographic microscopy

John Meshreki,* **Syed Muhammad Kazim, and Ivo Ihrke**

Chair for Computational Sensing and Communications Engineering, University of Siegen, Germany
*john.meshreki@uni-siegen.de

Abstract: Fourier ptychographic microscopy (FPM) is a recent technique to overcome the diffraction limit of a low numerical aperture (NA) objective lens by algorithmic post-processing of several low-resolution images. It can increase the space-bandwidth product of an optical system by computationally combining images captured under different illumination conditions. Vignetting determines the spatial extent of the bright and dark regions in the captured images. State-of-the-art analyses treat vignetting as a nuisance that needs to be reduced or excluded from algorithmic consideration using ad hoc decision rules. In contrast, this work investigates vignetting effects as a tool to infer a range of properties of the optical system. Generally, the goal of the FPM reconstruction algorithm is to achieve results that closely resemble the actual specimen at the highest resolution possible. However, as the optimization process does not necessarily guarantee a unique solution, we identify system properties that support alignment between computational predictions and empirical observations, potentially leading to a more accurate and reliable analysis. To achieve this, we characterize the individual system components of the experimental setup and compare experimental data to both, geometrical and wave optical simulations. We demonstrate that using vignetting as an analytical tool enables the modeling of the geometric and coherence properties of the optical system as evidenced by the good agreement between our simulation and experiment.

1. Introduction

FPM is an innovative method for achieving highly resolved 2D and 3D reconstructions [1–3] with a wide spectrum of applications in industry and biological and medical fields [4–6]. This is due to its efficiency in obtaining a high space-bandwidth product beyond the diffraction limit of the objective lens formulated by Ernst Abbe [7]. Moreover, FPM has been an inspiration for advances in other research areas in optics. For example, it has enabled an 8-fold resolution improvement in diffractive zone plate optics by using a diffractometer with sample rotations and a low-resolution binary zone plate, bypassing the fabrication challenges of small zone widths [8].

The FPM setup comprises an LED array, an objective lens, a tube lens, and a camera sensor to record the captured images, as shown in the ray optical simulation depicted in Fig. 1. By turning on one of the LEDs, it sends an electromagnetic field which interacts with the specimen placed in front of it. The wave exiting the specimen continues to propagate through the two lenses which magnify the image and a final image is recorded at the sensor plane. In the geometric optics paradigm, depicted in Fig. 1, this corresponds to a cone of light passing through the optical system and impinging on the camera sensor. We refer to the region inside the cone that reaches the sensor unimpeded by the limiting aperture of the optical system as the bright region and the region outside as the dark region.

In conventional microscope settings, with a constant space-bandwidth product, there is a trade-off between capturing high resolution information (high-NA) and a wide field of view (FoV, low-NA setting). In contrast, FPM overcomes this trade-off by using a low NA objective to

#543504 https://doi.org/10.1364/OPTCON.543504

Received 26 Sep 2024; revised 28 Oct 2024; accepted 28 Oct 2024; published 7 Nov 2024

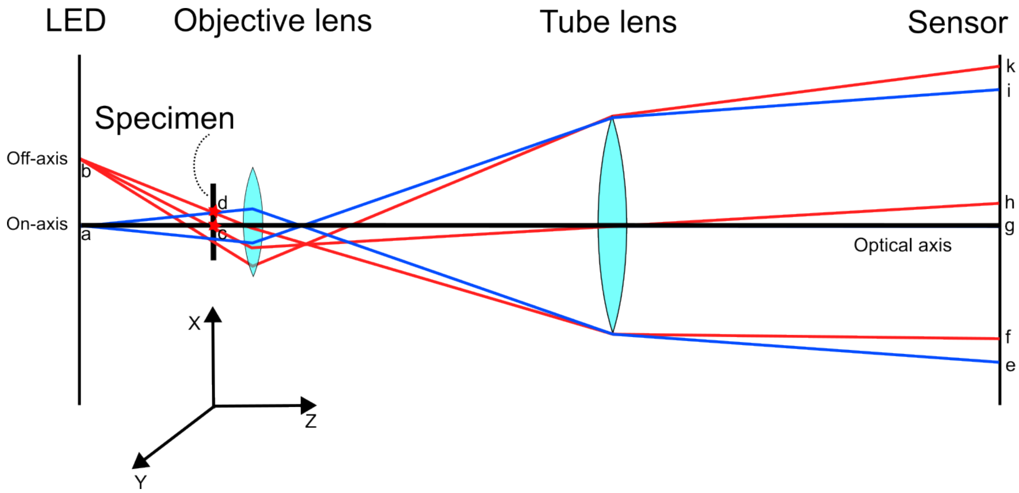

Fig. 1. A ray simulation of the FPM setup with X-Y planes representing the LED illumination, specimen, objective lens, tube lens, and sensor. The coordinate system of the setup is also displayed. The blue and red rays correspond to the on-axis and off-axis cases, respectively. Image regions within a cone of light are referred to as bright regions, whereas regions outside of it are dark regions.

capture multiple low-resolution, wide FoV images. Algorithmic post-processing then computes high-resolution, wide-FoV images, i.e. the space-bandwidth product is increased beyond that of the physical system. High-quality reconstructions require the knowledge of (1) first-order geometrical properties and (2) coherence properties of the system. Usually, this knowledge is inferred via additional optimization goals in the FPM reconstruction procedure [2]. Since the resulting optimization problem is nonlinear and nonconvex, it remains uncertain whether accurate values are being recovered using this process. In this work, we therefore aim to identify system properties that can be inferred from direct observations.

Obtaining high-quality reconstructions necessitates careful treatment of factors that introduce nonlinearities, leading to discrepancies between ideal simulations and the measured quantities in real FPM setups. Many works have investigated and accounted for these factors, including noise [9,10], aberrations [11], LED positional misalignments [12–15], miscalibration [16] and vignetting effects [17–20].

These nonlinearities hinder the optical system from being linear space-invariant, potentially leading to a degradation in the reconstruction quality. In this work, we focus on vignetting in order to understand its effects in an FPM setup, paving the way for improved treatment.

There are two types of vignetting: natural and artificial. Natural vignetting arises from a natural fall off in brightness for an off-axis image point. On the other hand, artificial vignetting results from the truncation of rays due to the finite extent of apertures or stops, leading to a decrease in the brightness towards the rim of the image. Throughout this work, we focus exclusively on the latter, i.e. artificial vignetting.

State-of-the-art approaches address vignetting by either mitigating its effects [20] or excluding it from algorithmic assessments through specifically designed ad hoc strategies. However, we adopt a novel perspective on vignetting as a characteristic property of the optical system that is easily accessible and that carries valuable information about the system that can be extracted by careful analysis. We show that the (1) geometric and (2) coherence properties of an optical system can be accurately characterized, enabling predictive simulation, see for example Fig. 8(b) . In addition, vignetting can be used for a suitable alignment of the optical system as we show later.

OPTICS CONTINUUM

2. Related work

In an ideal world, the 4-f imaging system used in FPM would exhibit linear space-invariance (LSI). This would mean that the system's response to a point source is uniform across the entire field of view, allowing for consistent image quality and predictable outcomes. However, real-world setups deviate from this ideal due to several practical limitations and complexities [18]. One significant challenge is aligning simulations with experimental results, particularly for semi-bright and semi-dark field images. These images are created using LEDs within the transition zone between bright and dark fields. In these areas, the assumptions of the LSI model are violated. Moreover, the resolution of the imaging system tends to decrease as one moves towards the edges of the image [17]. This nonuniform resolution is caused by optical aberrations, lens imperfections, and limitations in the imaging setup, which are more pronounced at the edge of the FOV. As a result, the LSI model, which assumes uniform resolution, is not valid across the entire image plane. Furthermore, apertures and/or stops cause vignetting, where the intensity of light decreases towards the edges of the image. This results in uneven illumination and image brightness, breaking the assumptions of the LSI model. Therefore, in real settings we ultimately end up with a linear space-variant (LSV) model instead.

According to [18] vignetting effects cannot be fully corrected by calibration techniques. However, the authors propose two remedies to address this issue for amplitude-based specimens. The first approach involves dividing the FOV into smaller patches, which is called block processing. When processing these smaller regions, it becomes more feasible to approximate the LSI model within each patch. The assumption is that the optical characteristics within a smaller area are more uniform, thereby adhering more closely to the LSI model. Of course, the smaller the patch, the closer it approximates the ideal LSI conditions. This approach would therefore allow for localized analyses and corrections that would be impractical over the entire FOV. Nevertheless, block processing alone is not sufficient because it cannot account for all residual imperfections. These imperfections are difficult to simulate and can cause the reconstruction algorithm to diverge, leading to inaccurate results. To address this issue, the authors introduce a second approach. This method involves identifying and removing imperfect regions within each patch from the reconstruction process. By excluding these outlier regions, the algorithm can achieve more accurate and stable results, minimizing the impact of imperfections on the overall reconstruction quality. Nonetheless, the authors of [18] argue that these approaches may result in inaccurate phase reconstructions, particularly when imaging phase-based specimens where phase information is more critical than amplitude.

Another work [19] adopts a different approach by modifying the simulation to mimic the transition regions between bright and dark fields. The authors include an exponential phase factor to better describe the field's propagation across a wide FOV based on the Fresnel wave propagation integral. This adjustment allows the field to propagate to the lens plane instead of the Fourier plane, resulting in more accurate calculations of the cropping operation by the lens aperture. However, this approach might not be as effective if there are LED misalignments or lens distortions that shift the apparent center of the diffracted field, which often occur in real FPM setups. While the authors attempt to correct these effects, they argue that the solution only works to a limited extent for off-axis patches when using low-magnification objectives.

A recent work [20] explores the use of features rather than intensities to overcome vignetting effects obtaining a stitch-free full-FOV reconstruction. The authors employ a forward model based on feature extraction using a gradient operator, which eliminates the need for block processing and stitching procedures in the reconstruction process. This technique enables high-speed data acquisition, recording a single slide within 4s.

OPTICS CONTINUUM

3. Experiment

For the purposes of this work, we analyze an FPM setup that was constructed in our lab as depicted in Fig. 2. The illumination unit in the experimental setup employs a programmable Adafruit 32x32 LED array, where each LED is controlled using an Arduino microcontroller to emit red, green, and blue (R,G,B) light with a spacing of 4mm between each LED. The setup uses a 10x 0.3NA infinity-corrected Nikon objective lens, combined with a 200mm focal length tube lens (Thorlabs TTL 200). We use a consumer-grade camera (Canon 5D mark II) due to its large sensor area as well as a high resolution of 5,634 × 3,753 pixels with a pixel size of 6.4μm. We capture images of the NBS 1963A Pattern using the (R,G,B) modes of the LEDs to measure the system magnification as shown in Fig. 2. The camera's large sensor is able to capture almost the full extent of the unvignetted area, visible as a circle containing the specimen.

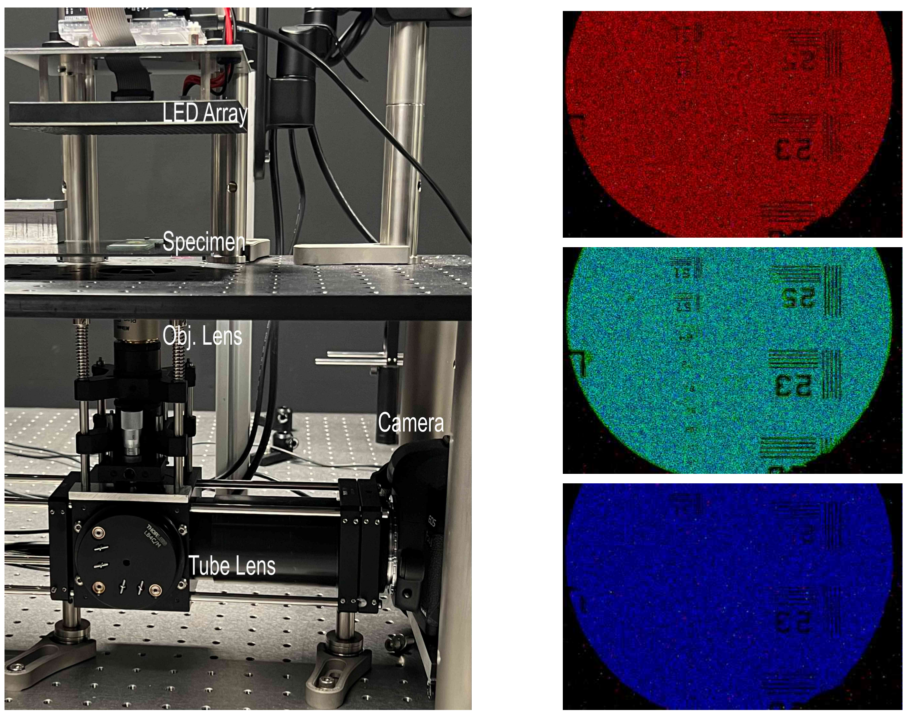

Fig. 2. (Left) Our FPM experimental setup. (Right) Low-resolution images of the NBS 1963A Pattern.

Moreover, we measure the spectral line shapes, see Fig. 3, and finite spatial extents of the tricolor (R, G, B) LED, see Fig. 4. Furthermore, pupil positions, principal planes and diameter extent are calculated for both the objective and tube lenses by running characterization experiments for the individual components and confirming the findings using optical design software. For focal lengths, we rely on the specifications of the manufacturer. These calculated physical parameters, in addition to the axial distances between individual components as well as the positions of the LEDs, are the input parameters to the microscope simulation.

OPTICS CONTINUUM

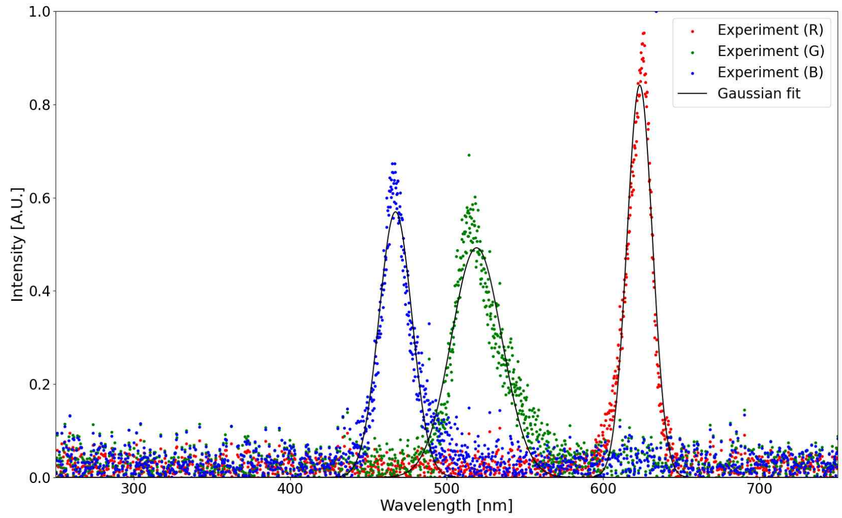

Fig. 3. Spectral lines for the LED modes (R, G, B) with Gaussian fits.

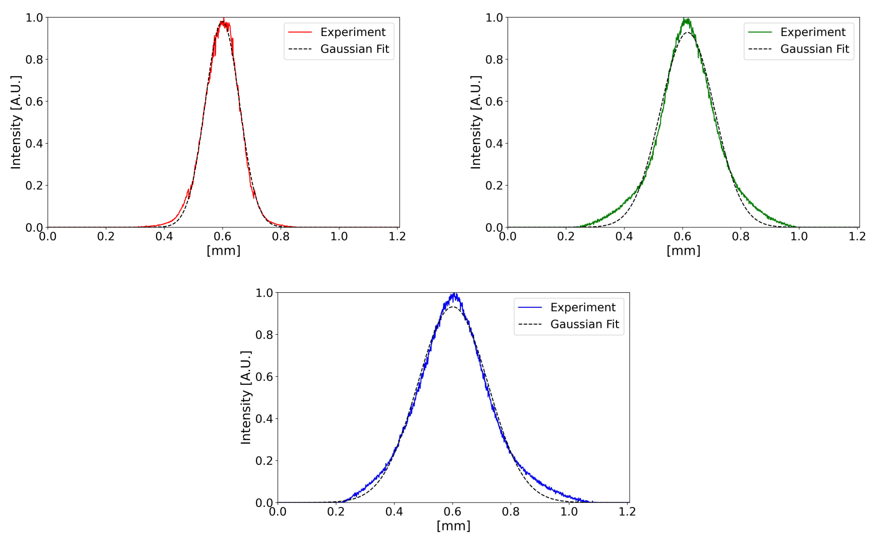

Fig. 4. Spatial emission profile of the (R,G,B) modes of the LED with Gaussian fits.

4. Image Processing

We capture images using red, green, and blue on-axis LEDs without a specimen, resulting in a bright circle surrounded by dark regions, see Fig. 5. This circle is referred to as the vignetting circle (VC) because it marks the boundary between the bright regions and the dark regions of the image due to vignetting. The absence of a specimen allows us to inspect the optical system exclusively from the VCs. In our setup for near-axis LEDs, this VC is caused by the tube lens restricting the propagation of light for on- and near-axis LEDs, see Fig. 1.

To analyze the vignetting effects, we extract an intensity profile along the edge of the VC for each color channel separately using image processing techniques. First, we observe that the geometric shape of the outer edge is elliptical rather than circular, suggesting a sensor tilt as explained in Sec. 5 and demonstrated in the bottom left of Fig. 6. For consistency, we continue

OPTICS CONTINUUM

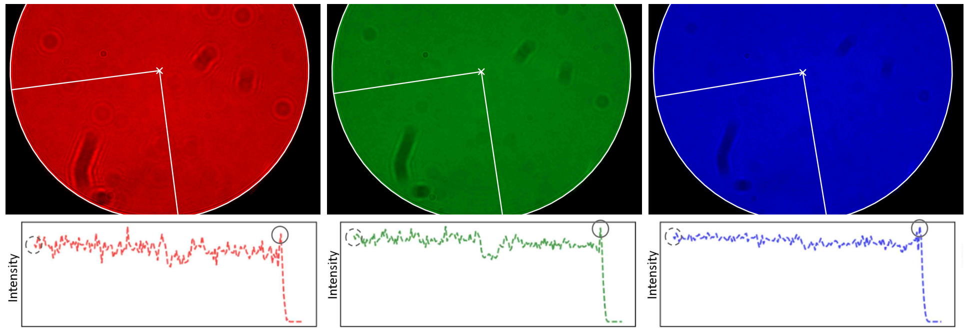

Fig. 5. (Top) Low-resolution images captured without a specimen, illuminated by (R, G, B) LEDs, each fitted separately with an ellipse. (Bottom) Scan lines from the center (dashed circles) to the boundary of the image through the edges/intensity maxima (solid circles) with R, G, and B illuminations.

to refer to it as the VC throughout this work. Second, we detect the intensity maxima along the edges of the VCs, generating a set of points along their respective boundaries, which we fit with ellipses, establishing their midpoints and major and minor axes. The midpoints, minor and major axes are overlaid on the measurements in Fig. 5.

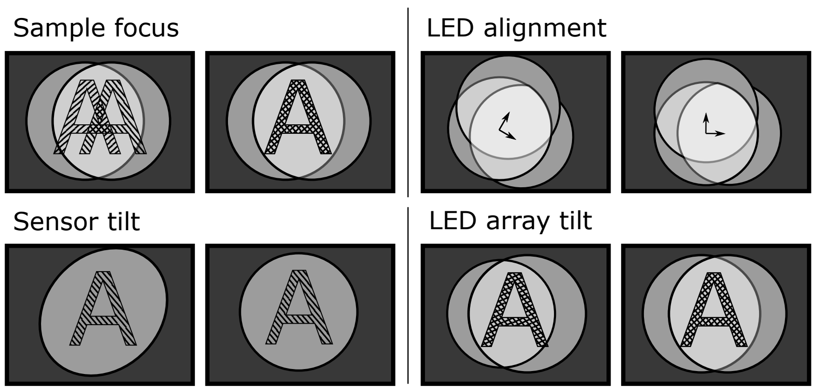

Fig. 6. Focusing (top left) and alignment (top right) can be finely adjusted activating multiple LEDs. Sensor and LED array tilts affect the eccentricity and relative scale of the VCs, respectively.

To observe the effects of interference on a VC, a scan line from the center of the ellipse (dashed circle) to the edge of the image is plotted for each illumination in Fig. 5 (bottom). Although the intensity maxima (solid circle) are identifiable, other plausible underlying patterns are concealed by noise. We mitigate the effects of noise by scaling the major and minor axes by a common factor to generate concentric ellipses, and averaging the intensities along the circumference of each ellipse. We thereby obtain a noise-reduced intensity value for each scale factor, resulting in the intensity profiles with interesting properties as shown in Fig. 8(b).

5. Alignment

A first advantage of studying vignetting lies in its usefulness for a suitable alignment of the optical system, see Fig. 6. If the sensor is chosen to be sufficiently large, the VC becomes visible in the image plane, separating bright and dark regions, see Fig. 5.

Assuming a sensor centered on the optical axis, e.g. with the aid of an alignment laser, the LED array can be centered by moving its center LED such that the VC is centered on the sensor. This is best done with live view capabilities.

For further system alignment, it is useful to activate several LEDs, e.g. in an “L” or cross pattern, see Fig. 6 (top right), since the orientation of the LED array with respect to the sensor axis becomes visible and can be adjusted accordingly. In addition, an out-of-plane tilt in the LED array manifests as a change in the VC’s radius (bottom right).

A second observation is that focusing the microscope with single LED illumination is difficult due to the near-coherent illumination and the corresponding small illumination NA, causing a very large depth of field. Activating multiple LEDs leads to the superposition of several specimen images (illustrated by the “A” pattern and assuming it to be planar) when the specimen is out of focus. Adjusting the focus shifts these copies with respect to each other, see Fig. 6 (top left). Therefore, a good focus setting is achieved when the multiple images are aligned on top of each other. For 3D samples, a suitable sample plane should be chosen as the reference focus in this manner.

In both the 2D and 3D cases, a larger lateral LED distance from the center leads to increased sensitivity. A sensor tilt is visible as an elliptical shape of the VC, Fig. 6 (bottom left). In case visual assessment does not suffice, ellipse-fitting methods can be employed as a post-processing step. The eccentricity of the ellipse and the comparison of major/minor axis lengths can be used as measures of alignment for sensor tilt and LED array tilt, respectively.

6. Geometric characterization

In the following, we aim to match a simulation to observed intensity images of the VC. In a first step, we exploit, as a second property of the VC, its sensitivity to the construction parameters of the optical system.

The analysis of the VC provides valuable information about the optical system. In particular, we consider the diameter and LED magnification of the VC in addition to the standard object magnification. The standard object magnification, denoted as M_{Obj}, is measured using the NBS 1963A resolution target.

The other two parameters are defined according to Fig. 1, which shows a first-order ray tracing simulation of the optical setup. The diameter of the VC, denoted as d_{VC}, is defined as:

$$d_{VC} = \overline{ei}, \tag{1}$$

which indicates the extent of the light distribution across the field of view as projected onto the sensor plane. In practice, we use the intensity maximum of the diffraction pattern as a reference point.

The LED magnification of the VC, denoted as M_{LED}, is calculated as the ratio of distances on the sensor and LED planes:

$$M_{LED} = \overline{gh}/\overline{ab}, \tag{2}$$

where a and b represent the LED positions and g and h denote the centers of the VC, i.e., the intersection points of the chief rays with the sensor plane. This step provides additional information about the displacement of the VC in response to the activation of an off-axis LED.

We formulate the determination of the optimal system parameters as an optimization problem: Given experimental values of the three observables, d_{VC}, M_{LED} and M_{Obj}, determine the most likely construction parameters of the system, i.e. the axial distances, component diameters, focal lengths, pupil and principal plane positions as well as lateral LED spacing. Collecting the geometrical observables in a vector $\boldsymbol{\phi}_g$ (outlined in Table 1) and the system parameters in a vector $\boldsymbol{\theta}_g$ (summarized in Table 2), and denoting a first-order ray optical simulation that is

OPTICS CONTINUUM

predicting the observables as $f_{geom}(\boldsymbol{\theta}_g)$, we may write

$$\boldsymbol{\theta}_g^* = \underset{\boldsymbol{\theta}_g}{\operatorname{argmin}} \left\| f_{geom}(\boldsymbol{\theta}_g) - \boldsymbol{\phi}_g \right\|_2^2, \tag{3}$$

where $\boldsymbol{\theta}_g^*$ is the vector of geometric system parameters causing the best fit between simulation and measurement.

Table 1. Comparison of the elements of $\boldsymbol{\phi}_g$: VC diameter and object and LED magnifications between simulations and measurements for the (R,G,B) LED modes.

Illumination	Type	d_{VC} [mm]	M_{obj}	M_{LED}
Red	Simulation	34.20	9.96	0.32
	Measurement	33.89	10.00	0.31
Green	Simulation	34.20	9.96	0.32
	Measurement	33.97	10.00	0.31
Blue	Simulation	34.20	9.96	0.32
	Measurement	33.99	10.00	0.30

Table 2. Optimized geometrical system parameters $\hat{\theta}_g^*$ of the FPM simulation. Note that *PP* refers to the Principal Plane.

Distances (planes) [mm]	LED to Specimen	66.49
	Specimen to Obj. Lens Object PP	20.00
	Obj. Lens Object PP to Tube Lens Image PP	185.48
	Tube Lens Image PP to Tube Lens Stop	26.68
	Tube Lens Stop to Sensor	173.88
Obj. Lens [mm]	Focal length	20.00
	Object PP diameter	12.60
Tube Lens [mm]	Focal length	200.00
	Image PP diameter	67.50
	Stop diameter	28.18

We begin the optimization process by initializing $\boldsymbol{\theta}_g$ with the corresponding measured parameters, and use an estimate of their standard deviations to perform a Monte-Carlo (MC) sampling in the vicinity of the initial guess, assuming independent Gaussian errors of the individual measurements to avoid local minima that may occur in our over-parameterized system. We then select the minimum and iteratively repeat the process with decreased standard deviation values. We did not observe multiple minima within the measurement uncertainties which suggests that a gradient descent optimization may be used in the future.

Using the optimized parameters $\boldsymbol{\theta}_g^*$ as input to the FPM simulation, we obtain a good agreement between the measured and simulated observables across all color channels as can be seen in Table 1. The table serves as a basis for the wave-optical simulation discussed in Sec. 7, where $\boldsymbol{\theta}_g^*$ are input to the next step – fitting the coherence properties of the system.

7. Wave-optical characterization

Given the geometric properties of the optical system, we upgrade the simulation to the scalar wave regime in order to match the coherence properties of the system between simulation and measurement. To achieve a more accurate comparison between measurements and simulations, we conduct a precise forward simulation based on the Rayleigh-Sommerfeld diffraction theory. This involves propagating electromagnetic fields emanating from a point source through the full FPM setup. The point source illumination is simulated by generating spherical wavefronts which propagate in free space. In contrast to the Fraunhofer formalism [21], our simulation emulates propagated fields for a relatively wide FoV with high accuracy due to the inclusion of a spherical phase term.

Suppose a spherical wave is generated from a point source on the LED plane located at $(x_0, y_0, -z_0)$ and we are interested in the phase profile at the specimen plane, where x_0 and y_0 are the X- and Y- coordinates and z_0 is the distance between the LED and specimen planes along the Z-axis. If we discretize the specimen along the X- and Y- axes, then the relative phase of the spherical wave at the specimen plane is given by:

$$e^{-jk\,\mathrm{sign}(z_0)\sqrt{(x_0-x_{\mathrm{sample}})^2+(y_0-y_{\mathrm{sample}})^2+z_0^2}}, \tag{4}$$

where x_{sample} and y_{sample} are the x- and y-positions of the discretized samples of the specimen, respectively. Note that $\mathrm{sign}(z_0)$ determines whether the wavefront is converging or diverging. In order to meet perfect imaging conditions, the phase modulation profiles of the lenses are adapted for different field points.

We use the angular spectrum method, as described by Matsushima et al. [22], to accurately model wave field propagation, which implements Rayleigh-Sommerfeld diffraction theory without approximation. Upon propagation through the lenses and arriving at the sensor plane, the final simulation image displays a distinct bright circle, encircled by darkness, a result of vignetting. To satisfy the Nyquist–Shannon sampling theorem [23] with respect to the number of discretized samples while also accelerating computations, the simulation is limited to two dimensions (2D), specifically within the X-Z plane, consequently, Eq. (4) is reduced to:

$$e^{-jk\,\mathrm{sign}(z_0)\sqrt{(x_0-x_{\mathrm{sample}})^2+z_0^2}}. \tag{5}$$

The apertures in the system give rise to prominent diffraction patterns at the edges of the VC, the detailed structure of which is related to a) the geometric system parameters, most notably the aperture size of the tube lens and the propagation distance to the sensor, and b) the coherence properties of the light source. We exploit this property by analyzing the diffraction pattern for the center LED in terms of the light source properties, see Fig. 8(b), and a refinement of the geometric system parameters, to establish the coherence properties of our FPM system.

We measure both the LED spatial emission profile and its emission spectrum for each color channel, by conducting a fit with a Gaussian function to extract the associated means and standard deviations μ_s, σ_s (spectral) and μ_x, σ_x (spatial), where μ_s, σ_s, μ_x and σ_x are determined for each of the (R,G,B) modes of the LED. The spectral lines and spatial emission profiles are shown in Fig. 3 and Fig. 4, respectively.

To simulate the partial coherence of the LED sources, we perform a MC sampling of the spatial $(\mu_x = 0, \sigma_x)$ and spectral probability distributions (μ_s, σ_s) determined by our measurements, where μ_x, σ_x, μ_s, and σ_s are individually treated for the (R,G,B) LED modes. Therefore, we vary the light source parameters based on the measured means and standard deviations and represent such coherence parameters as $\boldsymbol{\theta}_c = (\mu_s^r, \sigma_s^r, \sigma_x^r, \mu_s^g, \sigma_s^g, \sigma_x^g, \mu_s^b, \sigma_s^b, \sigma_x^b)$. The superscripts indicate the respective activated mode of the LED.

We simulate 1000 coherent fields with uniformly distributed random initial phases that are superposed incoherently. The individual simulations are initialized with spherical wavefronts in the specimen plane and propagated through the system, treating the microscope objective and the tube lens as thin lenses with a perfect lens phase profile that maps a divergent spherical wave from the point source to a spherical wave converging to its Gaussian image point. For first-order properties of the system, we use the optimized geometric system parameters $\boldsymbol{\theta}_g^*$. The simulation results in an intensity profile similar to the one labeled "Simulation" in Fig. 8(b), but generally not fitting the experimental curve precisely. We therefore resort to another optimization to fit the intensity profiles.

We adjust the $\boldsymbol{\theta}_g^*$ geometric parameters using a new variable $\hat{\boldsymbol{\theta}}_g$, while keeping it close to the previous result $\boldsymbol{\theta}_g^*$. Due to the wavy nature of the intensity profiles and the sensitivity of the curve to the light source parameters, it is not advisable to compare the curves directly. Instead, we opt for comparing the positions of the first four local intensity maxima (as seen from the step edge) across the profiles of all color channels. For the purpose of visualization, these maxima are highlighted in the blue plot at the bottom of Fig. 8(b). The positions are then collected in an observable vector, denoted as $\boldsymbol{\phi}_c$. Denoting the wave optical simulation and subsequent peak fitting as $f_{wave}(\boldsymbol{\theta}_c; \hat{\boldsymbol{\theta}}_g)$, we formulate the optimization as

$$\boldsymbol{\theta}_c^*, \hat{\boldsymbol{\theta}}_g^* = \underset{\boldsymbol{\theta}_c, \hat{\boldsymbol{\theta}}_g}{\operatorname{argmin}} \left\| f_{wave}(\boldsymbol{\theta}_c; \hat{\boldsymbol{\theta}}_g) - \boldsymbol{\phi}_c \right\|_{2,1} + \lambda \left\| \hat{\boldsymbol{\theta}}_g - \boldsymbol{\theta}_g^* \right\|_2^2, \tag{6}$$

where the group L2-norm is taken per LED. The standard deviation in the geometric parameters is iteratively reduced during optimization. The final fit is shown in Fig. 8(b), denoted as Simulation. Note that the results across the different LED modes utilize a single set of geometric system parameters. We have therefore obtained a single system description that can predictively simulate the diffraction behavior of our system at different wavelengths, as can be seen in Fig. 8(b). It is worth noting that the main peaks of the experiment show a slight tendency towards smaller amplitudes due to the averaging process applied along the ellipse circumference for noise reduction, see Sec. 4. The optimized parameters $\hat{\boldsymbol{\theta}}_g^*$ and $\boldsymbol{\theta}_c^*$ are summarized in Table 2 and Table 3, respectively.

Table 3. Optimized coherence parameters $\boldsymbol{\theta}_c^*$ of the FPM simulation.

Illumination	μ_s [nm]	σ_s [nm]	σ_x [mm]
Red	623.76	7.53	0.12
Green	519.67	12.06	0.16
Blue	468.96	6.66	0.15

Moreover, we calculated the temporal coherence length as follows [24]:

$$l_c = \sqrt{\frac{2\ln(2)}{\pi n}} \times \frac{{\lambda_0}^2}{\Delta\lambda}, \tag{7}$$

where n represents the refractive index of the medium (in our case, air with $n = 1$), and λ_0 and $\Delta\lambda$ denote the central wavelength and the full width half maximum of the wavelength, respectively. In our setup, considering green illumination, the temporal coherence length l_c is calculated to be $\approx 6.3\,\mu m$ (with $l_c \approx 9.3\,\mu m$ for blue and $l_c \approx 14.6\,\mu m$ for red). To convert this length to a lateral distance on the sensor we do the following. We model our optical system with a virtual LED, an exit pupil, and a sensor plane (without cascaded diffraction) assuming the tube lens is the limiting aperture as shown in Fig. 7. The LED acts as a point source in a virtual position, determined by first-order propagation into the image space. Image formation involves two main optical paths: the direct path $\overline{AC}$ and the path via diffraction at the exit pupil edge $\overline{AB} + \overline{BC}$. Next, we consider additional path differences due to the pupil function denoted as OPD(B) and OPD(E) at points B and E, respectively. Therefore, the total OPD between $\overline{AC}$ and $\overline{AB} + \overline{BC}$ can be formulated as

$$\text{OPD(total)} = [\overline{AC} + \text{OPD(E)}] - [\overline{AB} + \overline{BC} + \text{OPD(B)}]. \tag{8}$$

OPTICS CONTINUUM

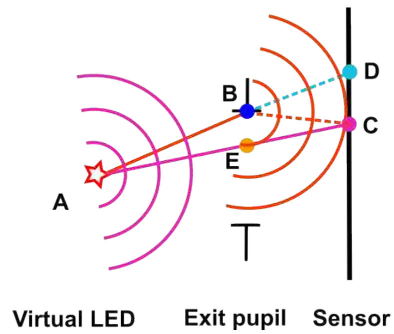

Fig. 7. Illustration depicting the conversion of the coherence length to a lateral distance on the sensor. Spherical waves propagating along the $\overline{\mathrm{AC}}$ path interfere with diffracted waves traveling along the $\overline{\mathrm{BC}}$ path at point C on the sensor. The lateral distance $\overline{\mathrm{CD}}$ marks the condition where OPD(total) equals l_c, with the former calculated using Eq. (9) and the latter determined by Eq. (7).

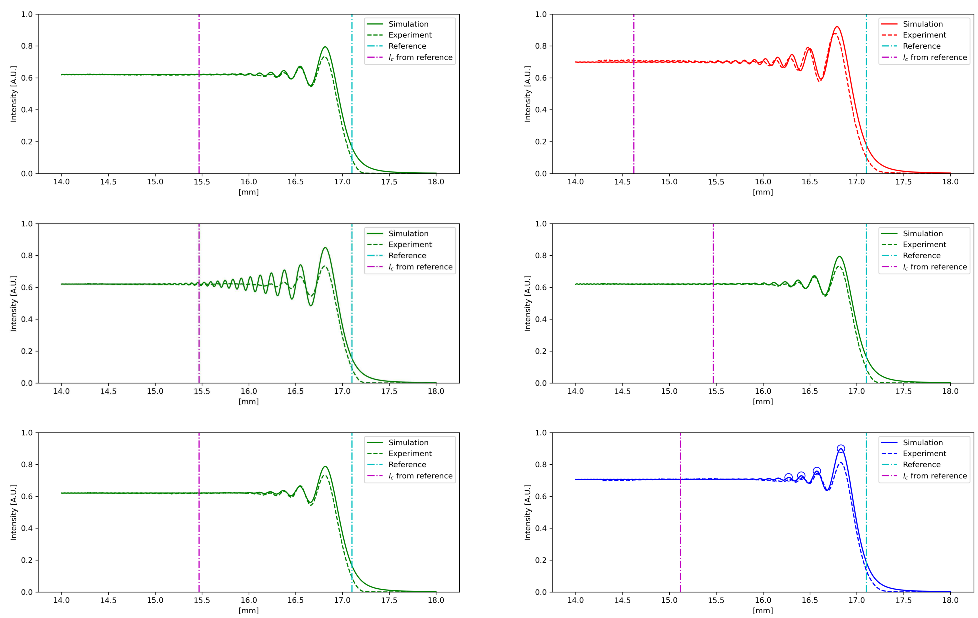

(a) Comparison of three different partial coherence simulations with measurements for the green LED: (top) spatial and temporal coherence, (middle) only temporal coherence, (bottom) only spatial coherence.

(b) Profiles of measurements and simulations for the (R, G, B) LED modes (top to bottom), with simulations incorporating spatial and temporal coherence. Circles in the blue subfigure highlight the first four peaks from the VC edge.

Fig. 8. The VC profiles of the measurements (dashed curves) are overlaid with the 1D simulations (solid curves). The cyan and magenta vertical lines indicate the extent of expected interference due to the temporal coherence length l_c of the respective wavelength, calculated using Eq. (7). These lines mark the reference points D and C in Fig. 7, representing the *Reference* and l_c *from reference*, respectively. Notice the peaks in the profiles extending to the left cease prior to l_c due to the influence of the spatial coherence.

However, OPD(B) and OPD(E) effectively cancel out, as points B and E are very close to each other and have nearly identical aberration contributions. Therefore, Eq. (8) is reduced to:

$$\mathrm{OPD(total)} = \overline{\mathrm{AC}} - [\overline{\mathrm{AB}} + \overline{\mathrm{BC}}]. \quad (9)$$

OPTICS CONTINUUM

To show l_c as a lateral distance on the sensor, we move point C away from D till the OPD(total) equals l_c. These points are highlighted in Figs. 8(a) and 8(b), where the reference point D is indicated by cyan lines (marking one quarter of the maximum intensity), and point C, where the total OPD equals l_c, is marked by magenta lines. We observe that the spatial extent of the light source has a non-negligible effect in reducing the interference region due to partial spatial coherence effects, which can be seen by the profiles in Figs. 8(a) and 8(b).

Using the parameters and methods outlined in the geometrical optics and scalar wave models (Secs. 6, 7), we compare our simulations to the measurements in Fig. 8(b), which displays the profiles for the R, G, and B LED modes. Our simulations show strong agreement with the measurements across all three color modes, using a single set of geometric system parameters while simultaneously modeling both temporal and spatial partial coherence. This validates vignetting as an effective analytical tool for modeling both geometric and coherence properties of the FPM optical system. Figure 8(a) highlights the effects of various partial coherence simulations for the green LED (results for the red and blue LEDs are available in the appendix). The temporal coherence simulation shows peaks extending further to the left compared to the corresponding measured profile, while the spatial coherence simulation results in shorter peaks. However, the simulation incorporating both spatial and temporal coherence aligns most closely with the measurements, demonstrating the best agreement.

8. Discussion

In addition to the observed vignetting caused by the tube lens, some far off-axis LEDs produce images with an additional vignetting edge caused by the objective lens. As a result, we observe double vignetting, where the intensity profile across one edge of the vignetting region is due to the tube lens and the other edge is influenced by the objective lens. It would be valuable to study such effects of the objective lens in greater detail to comprehensively understand all vignetting effects within the optical system, thereby deepening our understanding of this phenomenon.

It is worth noting that this work investigates an intriguing topic with relevance to various fields of optics, however, the complexity of this subject presents significant challenges. For instance, the forward model simulation is computationally intensive due to the large field of view and the Nyquist–Shannon sampling requirements [25]. Moreover, the authors of [18] argue that directly applying the LSV model to FPM reconstructions is difficult, if not impossible. This highlights the need for further research to deepen our understanding of these effects and to ultimately refine and improve the reconstruction process.

9. Conclusions

In conclusion, our investigation reveals that vignetting effects, often considered a nuisance in FPM, can be repurposed as a powerful tool for optical system characterization. By analyzing these effects, we can optimize the alignment of the optical system. This approach allows for accurate determination of the geometric construction parameters of the system. Additionally, vignetting analysis enables us to characterize the partial coherence properties, which are essential for accurately predicting interference effects in simulations. Our findings demonstrate that leveraging vignetting as an analytical tool would enhance the accuracy and reliability of FPM, bridging the gap between computational predictions and empirical observations.

Appendix

For completeness, we present the VC profiles of the measurements compared to our simulations for the blue and red LED modes (green mode is shown in Fig. 8(a)). As shown in Fig. 9, simulations incorporating both temporal and spatial coherence align more closely with the measurements than those simulating only temporal or only spatial coherence.

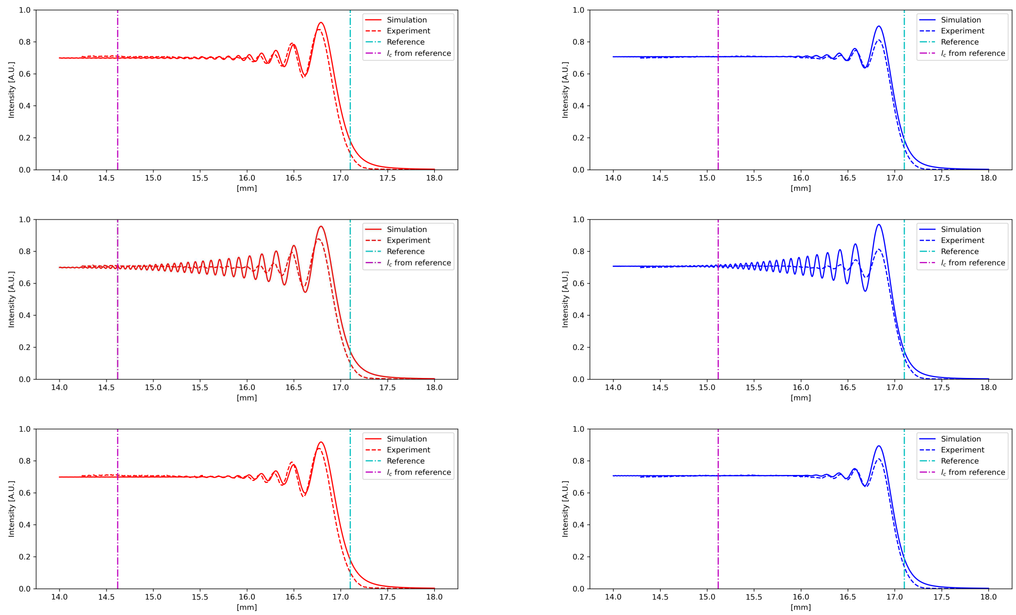

(a) Red LED. (b) Blue LED.

Fig. 9. The VC profiles of the measurements (dashed curves) are overlaid with the 1D simulations (solid curves) for the red (left) and blue (right) channels. The figures show a comparison of three different partial coherence simulations with measurement: (top) spatial and temporal coherence, (middle) only temporal coherence, (bottom) only spatial coherence. The cyan and magenta vertical lines indicate the extent of expected interference due to the temporal coherence length l_c of the respective wavelength, calculated using Eq. (7). These lines mark the reference points D and C in Fig. 7, representing the *Reference* and l_c *from reference*, respectively. Notice the peaks in the profiles extending to the left cease prior to l_c due to the influence of the spatial coherence.

Funding. Deutsche Forschungsgemeinschaft (FOR 5336, IH 114/2-1).

Disclosures. The authors declare no conflicts of interest.

Data availability. Data underlying the results presented in this paper are not publicly available at this time but may be obtained from the authors upon reasonable request.

References

1. G. Zheng, R. Horstmeyer, and C. Yang, "Wide-field, high-resolution Fourier ptychographic microscopy," Nat. Photonics **7**(9), 739–745 (2013).
2. L. Tian, X. Li, K. Ramchandran, *et al.*, "Multiplexed coded illumination for Fourier Ptychography with an LED array microscope," Biomed. Opt. Express **5**(7), 2376 (2014).
3. L. Tian and L. Waller, "3D intensity and phase imaging from light field measurements in an LED array microscope," Optica **2**(2), 104 (2015).
4. G. Zheng, C. Shen, S. Jiang, *et al.*, "Concept, implementations and applications of Fourier ptychography," Nat. Rev. Phys. **3**(3), 207–223 (2021).
5. C. K. Pavan, L. Loetgering, K. C. Zhou, *et al.*, "Fourier ptychography: current applications and future promises," Opt. Express **28**(7), 9603 (2020).
6. A. Pan, C. Zuo, and B. Yao, "High-resolution and large field-of-view Fourier ptychographic microscopy and its applications in biomedicine," Rep. Prog. Phys. **83**(9), 096101 (2020).
7. E. Abbe, "Beiträge zur Theorie des Mikroskops und der mikroskopischen Wahrnehmung," Archiv f. mikrosk. Anatomie **9**(1), 413–468 (1873).
8. C. Guo, S. Jiang, P. Song, *et al.*, "Bypassing the resolution limit of diffractive zone plate optics via rotational Fourier ptychography," Opt. Commun. **493**, 127031 (2021).

9. L.-H. Yeh, J. Dong, J. Zhong, *et al.*, "Experimental robustness of Fourier ptychography phase retrieval algorithms," Opt. Express **23**(26), 33214–33240 (2015).
10. C. Zuo, J. Sun, and Q. Chen, "Adaptive step-size strategy for noise-robust Fourier ptychographic microscopy," Opt. Express **24**(18), 20724–20744 (2016).
11. P. Song, S. Jiang, H. Zhang, *et al.*, "Full-field Fourier ptychography (FFP): Spatially varying pupil modeling and its application for rapid field-dependent aberration metrology," APL Photonics **4**(5), 050802 (2019).
12. C. Zheng, S. Zhang, G. Zhou, *et al.*, "Robust Fourier ptychographic microscopy via a physics-based defocusing strategy for calibrating angle-varied LED illumination," Biomed. Opt. Express **13**(3), 1581–1594 (2022).
13. Y. Chen, T. Xu, J. Zhang, *et al.*, "Precise and independent position correction strategy for Fourier ptychographic microscopy," Optik **265**, 169481 (2022).
14. R. Eckert, Z. F. Phillips, and L. Waller, "Efficient illumination angle self-calibration in Fourier ptychography," Appl. Opt. **57**(19), 5434–5442 (2018).
15. J. Sun, Q. Chen, Y. Zhang, *et al.*, "Efficient positional misalignment correction method for Fourier ptychographic microscopy," Biomed. Opt. Express **7**(4), 1336–1350 (2016).
16. V. Bianco, B. Mandracchia, J. Behal, *et al.*, "Miscalibration-tolerant Fourier ptychography," IEEE J. Sel. Top. Quantum Electron. **27**(4), 1–17 (2021).
17. R. Horstmeyer, R. Heintzmann, G. Popescu, *et al.*, "Standardizing the resolution claims for coherent microscopy," Nat. Photonics **10**(2), 68–71 (2016).
18. A. Pan, C. Zuo, Y. Xie, *et al.*, "Vignetting effect in Fourier ptychographic microscopy," Opt. Lasers Eng. **120**, 40–48 (2019).
19. M. Hasanzade, D. W. Breiby, and M. N. Akram, "Wide field-of-view Fourier ptychography microscopy based on Fresnel propagation scheme," Results Opt. **8**, 100259 (2022).
20. S. Zhang, A. Wang, J. Xu, *et al.*, "FPM-WSI: Fourier ptychographic whole slide imaging via feature-domain backdiffraction," Optica **11**(5), 634–646 (2024).
21. J. W. Goodman, *Introduction to Fourier Optics* (McGraw-Hill, New York, 1988), 2nd ed.
22. K. Matsushima and T. Shimobaba, "Band-limited angular spectrum method for numerical simulation of free-space propagation in far and near fields," Opt. Express **17**(22), 19662–19673 (2009).
23. C. E. Shannon, "A mathematical theory of communication," Bell Syst. Tech. J. **27**(3), 379–423 (1948).
24. Y. Deng and D. Chu, "Coherence properties of different light sources and their effect on the image sharpness and speckle of holographic displays," Sci. Rep. **7**(1), 5893 (2017).
25. M. Mout, A. Flesch, M. Wick, *et al.*, "Ray-based method for simulating cascaded diffraction in high-numerical-aperture systems," J. Opt. Soc. Am. A **35**(8), 1356–1367 (2018).